Two-dimensional full-wave simulations of waves in space and tokamak plasmas

E.-H. Kim,* N. Bertelli, E. Valeo, J. Hosea, and R. Perkins
Princeton Plasma Physics Laboratory, Princeton, New Jersey 08543

J. R. Johnson
Department of Engineering and Computer Science, Andrews University, Berrien Springs, Michigan 49103

(Dated: July 16, 2018)

We illustrate the capabilities of a recently developed two-dimensional full wave code (FW2D) in space and tokamak plasmas by adopting various values of density, magnetic field configuration and strength as well as boundary shape. As example, we first showed fast compressional wave propagation in the inner magnetosphere is dramatically modified by a plasmaspheric plume at Earth's magnetosphere. The results show that wave energy is trapped in the plume showing a leaky eigenmode-like structure with plume, which is similar to the detected magnetosonic waves. We also performed simulations of high harmonic fast waves in the scrape-off layer (SOL) plasmas of the National Spherical Torus eXperiment (NSTX)/NSTX-Upgrade. Comparison the results with previous full-wave simulations show that although the FW2D code uses a cold plasma approximation, the electric field and the fraction of the power losses in the SOL plasmas show excellent consistency and agreement with the previous full wave simulations performed by the AORSA code.

PACS numbers: 52.25.Os, 52.35.Hr, 52.50.Qt, 94.30.cv, 94.30.Tz

I. INTRODUCTION

In the solar system, many planets and their moons are magnetized and interaction of the solar wind with planetary magnetospheres leads to the formation of large scale field-aligned currents along with various electrostatic and electromagnetic waves.

There are many numerical efforts to understand plasma waves in planetary magnetospheres. Many models in the magnetosphere are based on WKB-based methods [e.g., 1, 2]. While these models can follow the flow of energy due to a particular excited wave, this approach is invalid for wave mode conversion or tunneling effects. On the other hand, a time-dependent fluid wave model has been used for waves in a wide range of frequencies [e.g., 3, 4]. Although they successfully demonstrated magnetospheric wave phenomena including mode conversion, the magnetic field curvature effect could not be captured because they adopted slab geometry. Hybrid wave simulation codes [e.g., 5, 6] and MHD fluid wave codes [e.g., 7] have also been used, however, they are numerically expensive or can only be used for limited frequency range.

A two-dimensional full-wave code, so-called FW2D, has been developed [8] to overcome those shortcomings. This wave code solves cold-plasma wave equations using the finite element method and an unstructured triangular mesh. It can easily describe wave propagation, mode coupling for arbitrary plasma by adopting various magnetic field configurations and geometries. Furthermore, a cold plasma approximation is useful to determine wave behavior in space as shown in previous simulations [e.g., 7], thus the model is well suited to address key science questions regarding the spatial distribution, frequency, and polarization of the various wave modes in space.

For instance, the FW2D code has been used to describe low frequency waves in Earth and Mercury's multi-ion magnetospheres [8–10]. The results include the generation and propagation of externally driven ultra-low frequency waves via mode conversion at the ion-ion hybrid resonance in Mercury and Earth's magnetospheres [8, 10] and mode coupling, refraction and reflection of internally driven field-aligned propagating left-handed EMIC waves at Earth [9].

More recently, the FW2D code has also been successfully adopted to tokamak geometry [10] to examine waves in the scrape-off layer (SOL) in the region of the plasma between the last closed flux surface (LCFS) and the tokamak vessel. This code is ideal for waves in the SOL plasma, because realistic boundary shapes and arbitrary density profiles can be adopted in the code and the SOL plasma can be approximated as a cold plasma.

Understanding of the interaction between radio frequency (RF) antennas and the SOL plasma is crucial because significant fractions of the coupled power can be absorbed in the SOL instead of the core plasma as desired. In particular, recent experimental studies employing high harmonic fast wave (HHFW) heating on the National Spherical Torus eXperiment (NSTX) [11, 12] has shown that substantial HHFW power loss (up to 60% of the power coupled from the antenna) can occur along the open field line in the SOL [13–17].

Many numerical simulations examine RF waves in tokamak by adopting a simulation domain that contains the SOL and plasma core [18–23]. Using AORSA (All order spectral algorithm) [24] code, Ref. [19, 20] particularly showed that power losses in the SOL start to increase significantly, commensurate with the amplitude

* ehkim@pppl.gov

of the RF field, when evanescent waves begin propagating in the SOL due to higher density in front of the antenna. Their results showed a good consistency with NSTX experiments [13, 14] although they assumed rectangular vessel shape.

In this paper, we illustrate the capabilities of the FW2D code. In addition to previous examples of waves in space plasmas [8–10], we demonstrate trapping of fast compressional waves power in plasmaspheric plume structures. We also examine HHFW in the SOL of NSTX and NSTX-Upgrade (NSTX-U) [25] by adopting various vessel shapes. By comparing the simulation results with previous full-wave simulation from AORSA [19], we verify capabilities to simulate tokamak plasmas beyond space plasmas.

This paper is structured as follows: a brief summary of the FW2D code is described in Section II. Sections III and IV contain two-dimensional full-wave simulation results of fast compressional wave propagation in the magnetosphere and NSTX/NSTX-U tokamak plasmas, respectively. The last section contains a summary.

II. FW2D MODEL DESCRIPTION

We developed a finite element wave code appropriate for general geometries [8, 10]. The code currently solves the cold plasma wave equations in two dimensions. Assuming time dependence, $\exp(-i\omega t)$, the linear and cold plasma wave equation takes the form,

$$\nabla \times (\nabla \times \mathbf{E}) - \left(\frac{\omega}{c}\right)^2 \boldsymbol{\epsilon} \cdot \mathbf{E} = 4\pi i \frac{\omega}{c^2} \mathbf{j}_{ext}, \qquad (1)$$

where $\mathbf{E}$ is the perturbed electric field, $\omega = 2\pi f$ is the wave angular frequency, c is the light speed, $\boldsymbol{\epsilon}$ is the dielectric tensor and $\mathbf{j}_{ext}$ is the external current source. A collisional frequency (ν) can be implemented in the momentum equation, then the plasma (ω_p) and cyclotron (ω_c) frequencies can be replaced with

$$\omega_{p(c)} \rightarrow \frac{\omega_{p(c)}}{1 + i\nu/\omega}. \qquad (2)$$

The collisions can be adopted near a simulation boundary to provide for absorbing boundaries or be added in the simulation domain to represent an ad-hoc model for wave dissipation and/or absorption as shown in Ref. [8].

The dielectric tensor $\boldsymbol{\epsilon}$ is expressed in coordinates aligned along and across the local ambient magnetic field direction $\hat{\mathbf{b}} \equiv \mathbf{B}/|\mathbf{B}|$, where $\mathbf{B}$ is an ambient magnetic field. For an axisymmetric plasma model, Eq. (1) can be expressed in cylindrical (r, z, ϕ) coordinates and all variables are represented as a superposition of Fourier modes with dependence $\exp(in_\phi\phi)$, where n_ϕ is the toroidal wave number.

The electric field $\mathbf{E}$ is represented in terms of its projections along ($\hat{b}$) and perpendicular ($\hat{\xi}, \hat{\eta}$) to $\mathbf{B}$. For magnetospheric dipole magnetic field, we define $\hat{\xi} \equiv \hat{\phi}$ with the assumption of $\mathbf{B} \cdot \hat{\phi} = 0$ [8] while $\hat{\xi} \equiv \hat{r} \times \hat{b}$ for tokamak geometry [10]. We also define $\hat{\eta} \equiv \hat{b} \times \hat{\xi}$ to complete the orthogonal coordinate. Thus the electric field can be described to

$$\mathbf{E}(r, z) = \sum_{n_\phi} \left(E_b \hat{b} + E_\eta \hat{\eta} + E_\phi \hat{\phi} \right) \exp(in_\phi \phi). \qquad (3)$$

Eq. (1) has been solved on an unstructured triangular mesh. We represent the variation of the electric field within each triangle by vertex-based linear finite elements local basis function, $F_{j,k}$, where j labels each triangle and k = 1, 2, 3 labels each of its vertices. The $F_{j,k}$ varies linearly between 1 at the k^{th} vertex and 0 at the other vertices, and is identically 0 outside triangle j, thus the electric field is

$$E = \sum_{j,k} E_{j,k} F_{j,k}. \qquad (4)$$

Then Eq. (1) is cast into matrix form by taking its inner product in turn with each $F_{j,k}$, and integrating by parts to obtain the weak variational form (see for example of Ref. [26])

$$\int d\phi r dr dz \{(\nabla \times \mathbf{F}^*_{j,k}) \cdot (\nabla \times \mathbf{E}) + \mathbf{F}^*_{j,k} \cdot \epsilon \cdot \mathbf{E} + i4\pi \frac{\omega}{c^2} \mathbf{F}^*_{j,k} \cdot \mathbf{j}_{ext}\} = 0. \qquad (5)$$

Substitution of Eq. (4) into Eq. (5) yields a sparse matrix system that is amenable to solution by standard algorithms. To take advantage of the sparseness of the matrix system, we employed a Gibbs algorithm [27] to reorder the mesh to minimize the bandwidth of the matrix.

One advantage of using the finite element method is that the local basis functions that are employed can be readily adapted to boundary shapes and can be packed in such a way as to provide higher resolution in regions where solutions may exhibit singular behavior. Where the geometry is more complex (near the boundary and near singularities) the wave solution needs to be resolved by small elements to give good global accuracy.

Moreover, the density of the mesh can be specified based on the expected wavelength obtained from solution of the local dispersion (except close to resonances) so that the most efficient resolution can be used. We generated the mesh by using an adoption of DISTMESH [28] or TRIANGLE [29] algorithms. The algorithms construct 2D triangle meshes for given specific boundaries and target density function. These mesh algorithms are particularly useful because it allows us to pack extra resolution where waves propagate with fine small wavelength (See Figure 1(d)).

III. FAST COMPRESSIONAL WAVES IN EARTH MAGNETOSPHERE

It is well known that the plasmaspheric plasma can expand beyond the plasmapause in the form of the dense

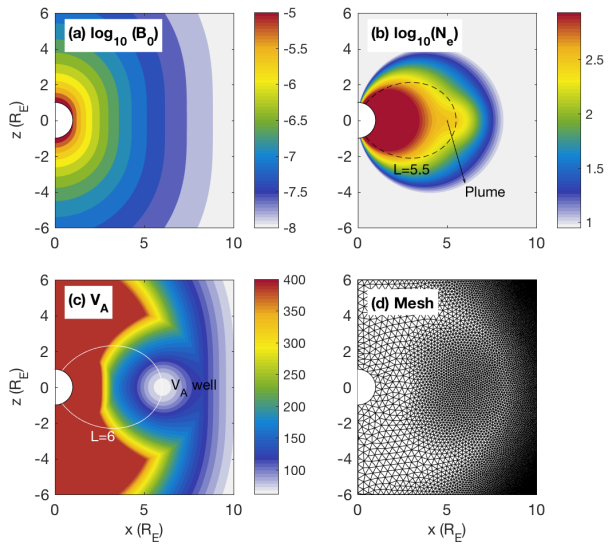

FIG. 1. The adopted plasma parameters for fast compressional wave simulations of $\omega = 2\pi f = 0.1$Hz. (a) The ambient magnetic field (T), (b) the electron density (m^{-3}) based on plasma density model [30] with the addition of a plasmaspheric plume added at 5.5 R_E, (c) The Alfvén velocity (V_A) calculated using given magnetic field and the density, and (d) the density of the mesh specified based on the expected wavelength obtained from the solution of the local dispersion.

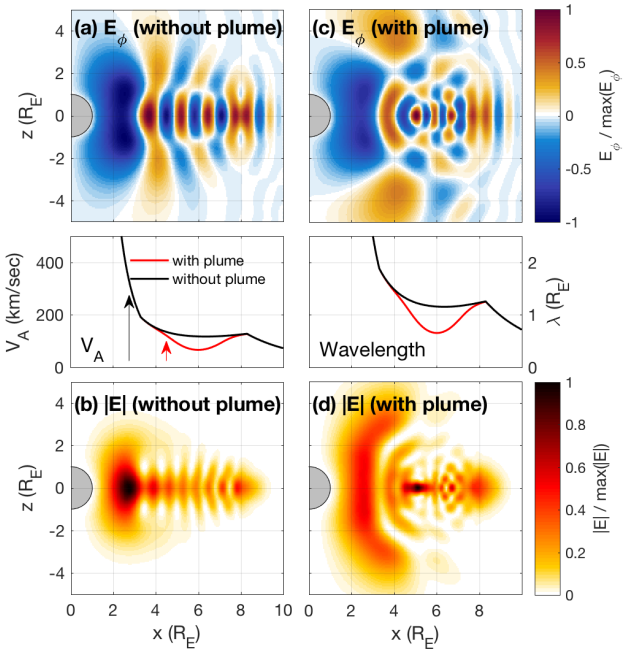

FIG. 2. Wave solution of the azimuthal electric field E_ϕ and the total electric field amplitude $|E|$ for a $\omega = 0.1$Hz fast compressional wave, which is launched at 8 R_E (a-b) without and (c-d) with plume. Without plume, the waves reflect and maximum wave power occurs at plasmaspheric boundary, however, with plume wave energy is trapped in the plume when the plume exists. Wave power with plume is much weaker than without plume and this is evident the wave energy is leaky well with plume. The Alfvén velocity profile and the wavelength at the magnetic equator also plotted in this figure. Here the arrows in Alfvén velocity profile indicate wave reflection locations, i.e., plasmaspheric boundary where the plasma density and Alfvén velocity tend to be steeper.

blobs, the plume (see Figure 1 of Ref. [31]). In order to consider the effects of plasmaspheric plume on wave propagation, we have examined two-dimensional propagation of fast compressional waves in a magnetospheric dipole geometry as an example of the utility of FW2D code.

For the ambient field, we have taken a dipole as shown in Figure 1(a). The adopted electron density profile is also in Figure 1(b). The inner magnetospheric density model used in this calculation is based on the observational studies [30, 32], while a background density of 1cm^{-3} is imposed in the outer magnetosphere.

In order to examine the plume effects on wave propagation, we consider cases with and without a density plume localized near $L = 5.5$, where L is a parameter which at the magnetic equator corresponds to the radial distance from the Earth's center expressed in units of Earth radius (R_E) [33]. The Alfvén velocity (V_A) is calculated using given magnetic field and the density as shown in Figure 1(c). Here, it is clearly shown that the plume provides a local reduction of V_A, hence Alfvén velocity well appears near $L = 6$. The density of the mesh can be specified based on the expected wavelength obtained from the solution of the local dispersion. Since we prescribe that the wave frequency of $f = \omega/2\pi = 0.016$Hz is lower than the ion cyclotron frequency of $f_{ci} = \omega_{ci}/2\pi = 0.3$Hz at $L = 8$ in the magnetic equator in electron-proton plasma, the wavelength (λ) of the fast compressional wave can be approximated as

$$\lambda \propto \frac{V_A}{\omega}, \tag{6}$$

thus the mesh density is proportional to V_A as shown in Figure 1(b).

Because we assume that all waves at the ionosphere totally reflect, which is similar to the previous time-dependent MHD simulation [7], reflecting boundary conditions are prescribed at the Earth's surface, while absorbing boundary conditions are adopted at all other boundaries.

Figure 2 shows the wave solutions of the azimuthal electric field component (E_ϕ) and the total electric field strength ($|E|$) with and without plasmaspheric plume for $f = 0.016$Hz. A large-scale compressional wave is launched in $J_{\phi,ext}$ at 8 R_E in the model. The wave propagates away from the source both earthward and tailward. The equatorial Alfvén speed and wavelength profile along radial direction are also plotted in this figure. The tailward traveling wave propagates to the boundary where it

is absorbed, so it does not affect the solution in the inner magnetosphere. As waves propagate into the inner magnetosphere, they are refracted away from the earthward Alfvén velocity gradient leading to enhanced wave power at the equatorial plasmaspheric boundary where both V_A and density profile tend to be steeper in the inner magnetosphere. Existence of the plasmaspheric plume pushes the location where the wave power enhancement occurs to outer magnetosphere, for instance, it occurs at $L \sim 5$ with plume and $L \sim 2.5$ without plume as shown in Figure 2.

It is also apparent that when the plume exists wave energy is trapped in the 'Alfvén velocity well' and forms a leaky eigenmode-like structure with plume, while waves propagate as plane waves in the case without the plume. This trapping of wave energy in the plasmaspheric plume also affects how much magnetosonic wave energy can reach the plasmaspheric boundary, where wave energy accumulates as the wave reflects. In addition, Figure 2 shows that wave energy without the plume near the plasmaspheric boundary is much stronger than wave energy with the plume. It is evident that the plasma plume sucks in the wave energy shadowing the plasmaspheric boundary from the pile-up of wave energy seen in the case without the plasma plume.

IV. FAST WAVE PROPAGATION IN THE SOL OF NSTX/NSTX-U

In order to show and benchmark the new FW2D capability to simulate RF wave in tokamak plasma, we adopt the plasma equilibria of NSTX and NSTX-U, which has been used for AORSA wave simulations [19]. In particular, for NSTX-U, we analyze a projected of H-mode scenario with $B_{\rm T} = 1$T obtained by the TRANSP code [34, 35].

The outer boundaries are assumed to be perfectly reflecting, which is different from the boundary condition of Section III, and collisions are included in the plasma core to absorb all waves. Thus the plasma absorbs all incoming wave energy without energy loss at the boundaries and this enables us to estimate the collisional power losses both in the plasma core and SOL when artificial collisions are considered.

We perform simulations using single toroidal mode numbers, $n_\phi = -12$ or -21, which correspond to an NSTX/NTSX-U antenna phase of $-90°$ or $-150°$, respectively, and various densities in front of the antenna ($N_{\rm ant}$). The waves are launched with wave frequency of $f = 30$MHz. We use the same density profile as Ref. [19] (see Figure 1 of Ref. [19]) assuming that the electron density in the SOL is exponentially decaying.

Figure 3 shows the total electric field amplitudes ($|E|$) as well as the left- ($|E_+|$) and right-handed ($|E_-|$) wave electric field amplitudes obtained by FW2D (first row) and AORSA (second row) for $n_\phi = -12$ and $N_{\rm ant} = 1 \times 10^{18}{\rm m}^{-3}$ in NSTX. In this figure, we also plot the

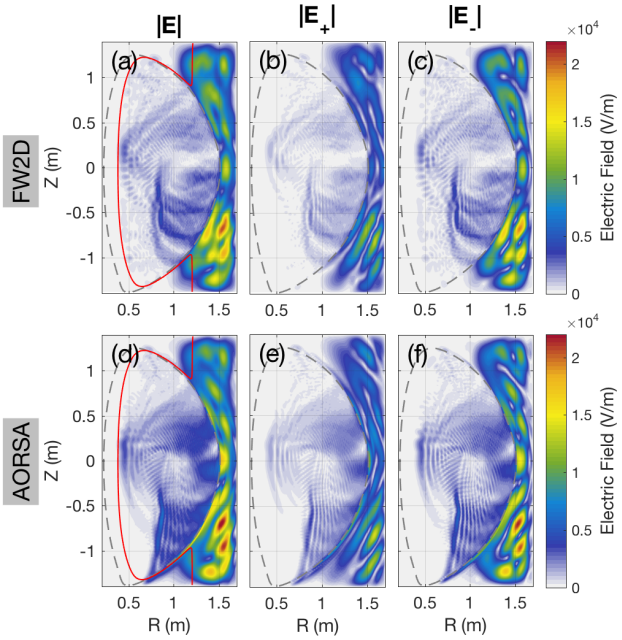

FIG. 3. The electric field amplitude in NSTX shot 130608 for different wave polarizations, such as total ($|E|$) as well as left- ($|E_+|$) and right-handed ($|E_-|$) polarizations, with toroidal mode number $n_\phi = -12$, electron density in front of antenna $N_{ant} = 1 \times 10^{18} m^{-3}$, and $\omega/2\pi = 30$MHz using (a-c) FW2D and (d-f) AORSA codes, respectively. The black dashed and red solid curves indicate the LCFS and FW cutoff layer, respectively. Here, R and Z are radial and poloidal (vertical) directions.

LCFS (dashed black curves) and the fast wave (FW) cutoff layer (red curves). Here, simulation results from AORSA are reproduced from Ref. [19]. FW2D results in Figure 3 are in excellent agreement with AORSA. We also examine HHFW propagation using various densities in front of the antenna. Figure 4 show the wave electric field amplitude from FW2D and AORSA for a single toroidal mode $n_\phi = -21$ and various densities in front of antenna, $N_{\rm ant} = 1$, 2, and $3 \times 10^{18}{\rm m}^{-3}$, respectively. When the FW cutoff is 'closed' in front of the antenna and the waves are evanescent as shown in Figure 4(a), the small RF field amplitude in the SOL remains localized near the antenna. When $N_{\rm ant}$ increases sufficiently to 'open' the FW cutoff in front of the antenna as shown in Figure 4(b), the wave amplitude in the SOL strongly increases showing a standing wave structure, as previously found in simulation from AORSA in Figure 4. Simulations for NSTX-U have been also performed (not shown here) and the results lead to the same conclusions in agreement with previous results [19, 20].

The fraction of power losses in the SOL ($P_{\rm abs}$) can be defined as a ratio between total power absorbed to the

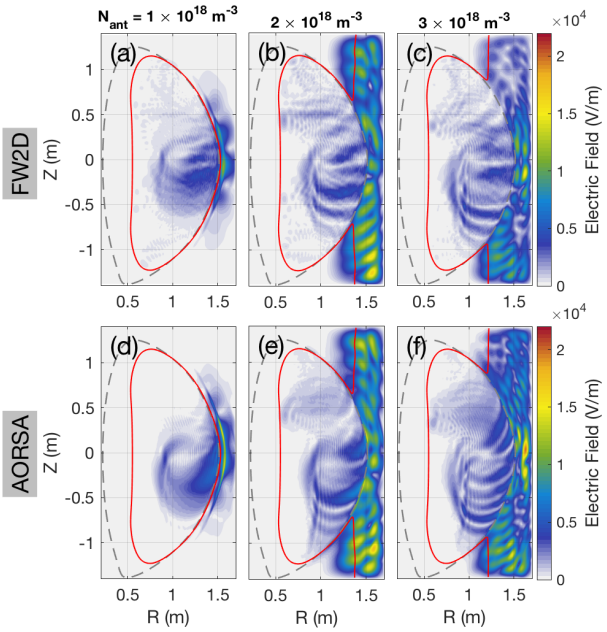

FIG. 4. Total electric field amplitude in NSTX shot 130608 using (a-c) FW2D and (d-f) AORSA code for different density values in front of the antenna (shown in the plots) with toroidal mode number $n_\phi = -21$.

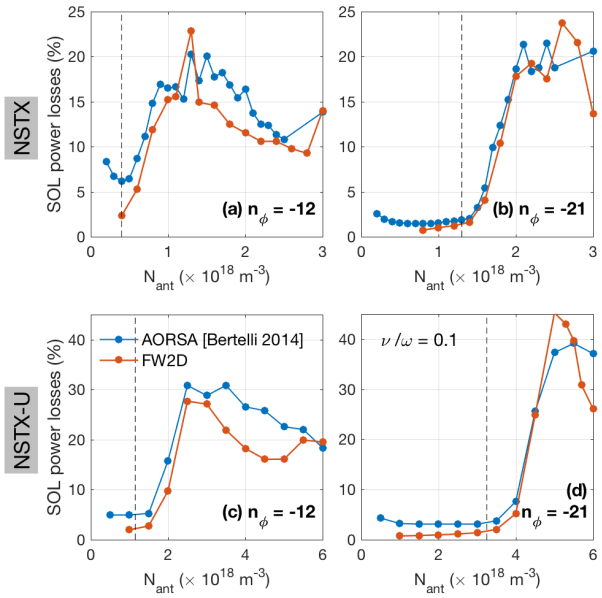

FIG. 5. Fraction of power lost to the SOL ($P_{\rm abs}$) of (a-b) NSTX and (c-d) NSTX-U calculated by FW2D and AORSA as a function of the density in front of the antenna ($N_{\rm ant}$) for $n_\phi = -12$ and -21. The vertical lines represent the critical density ($N_{\rm ec}$) at which the cutoff starts to be open in front of the antenna. Here calculation from AORSA are reproduced from Ref [19].

plasma ($W_{\rm tot}$) to power loss in the SOL ($W_{\rm SOL}$),

$$\text{SOL power loss } (P_{abs}) = \frac{W_{\rm SOL}}{W_{\rm tot}}. \tag{7}$$

For FW2D code, because it adopts a cold plasma approximation, power losses in the plasma core and SOL have been calculated by adopting artificial collisional effects, which cause all incoming wave power to be absorbed in the plasma. Thus power losses can be calculated as $W_{\rm SOL} = \int_{\rho_{\rm pol}>1} \mathbf{J}\cdot\mathbf{E}^* dV$ and $W_{\rm tot} = \int \mathbf{J}\cdot\mathbf{E}^* dV$, where V, $\mathbf{J}$, and $\rho_{\rm pol}$ are the volume, the perturbed current density, and the square root of the normalized poloidal flux, respectively. On the other hand, the AORSA code includes the plasma kinetic effects. Therefore the power absorption in the plasma core is evaluated by the Landau damping and transit-time magnetic pumping. Artificial collisions, however, has been implemented in AORSA as well to estimate the power losses in the SOL plasma (see Ref. [19] for additional details).

Figure 5 showed the predicted $P_{\rm abs}$ using FW2D and AORSA as a function of $N_{\rm ant}$ assuming $\nu/\omega = 0.01$ [19] for NSTX (a-b) and NSTX-U (c-d). Despite the discrepancy of methodology to calculate $P_{\rm abs}$ between AORSA and FW2D codes, the results show very good agreement. The vertical lines in Figure 5 represent the critical density ($N_{\rm ec}$) at which the cutoff starts to be open in front of the antenna, which is proportional to the ambient magnetic field [13, 14, 19, 20]. Showing good agreement with AORSA, $P_{\rm abs}$ sharply increases and reach the maximum value when $N_{\rm ant}$ is slightly larger than $N_{\rm ec}$. The maximum loss occurs when the electric field amplitude in the SOL is enhanced [19, 20] as shown in Figure 4.

We also scanned $P_{\rm abs}$ for various value of ν/ω (Results are not shown here) and we found that $P_{\rm abs}$ increases basically linearly as ν/ω increases, thus the general behavior of $P_{\rm abs}$ does not change varying ν, which is consistent with Ref. [20].

Because the FW2D code uses the finite element method and an unstructured mesh, this code easily adopts various boundary shapes. In addition to the rectangular boundary shape, we adopt a vacuum vessel boundary as shown in Figure 6. Here, except the boundary, all plasma parameters are the same as the simulations in rectangular boundary shape from Figure 3 for $n_\phi = -12$ and $N_{\rm ant} = 1\times10^{18}{\rm m}^{-3}$ and Figure 4(b) for $n_\phi = -21$ and $N_{\rm ant} = 2\times10^{18}{\rm m}^{-3}$. Figure 6 clearly shows that wave propagation behavior in the SOL strongly depends on the boundary shape. Since the launched waves at the antenna propagate through the SOL and reach the plasma core, wave solution in the plasma core are also affected by the boundary shape. In Figure 6, the FW cutoff is open because of the $N_{\rm ant}$ exceed the critical density $N_{\rm ec}$. However, unlike Figure 3 and Figure 4(b) where standing mode structure of the FW mode appear in Figure 6, the waves are strongly localized near the antenna without standing mode structure. Therefore, these initial results suggest that the use of a realistic vessel boundary might play an important

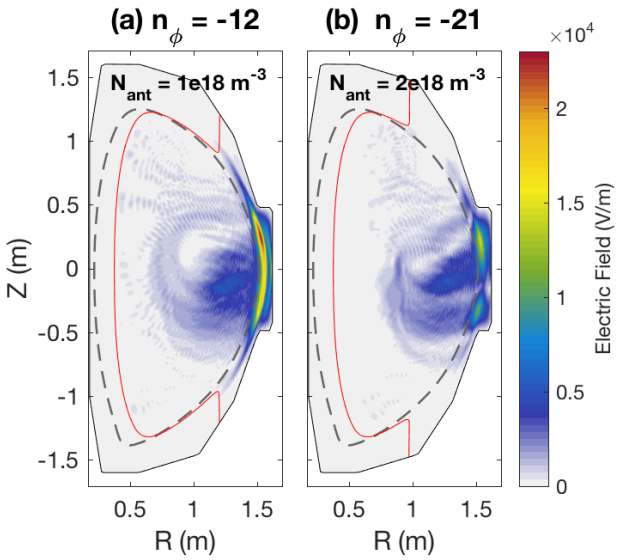

FIG. 6. Two-dimensional electric field amplitude from FW2D code with a vacuum vessel boundary for (a) $n_\phi = -12$ and $N_{\rm ant} = 1 \times 10^{18}{\rm m}^{-3}$, which is the same condition as Figure 3 and (b) $n_\phi = -21$ and $N_{\rm ant} = 2 \times 10^{18}{\rm m}^{-3}$, which is the same as Figure 4(b), respectively.

role and a detail numerical investigation on this aspect is necessary. A more comprehensive work on this specific topic will be part of a separate paper.

V. DISCUSSION AND SUMMARY

A two-dimensional full-wave (FW2D) code using the finite element method has been developed to understand plasma wave behavior in space and tokamak plasmas. In this paper, we show the capability of the code for both space and tokamak plasmas. We successfully demonstrate plasma waves in a wide range of simulation domain scale ($1.5{\rm m} - {\rm R_E}$), magnetic field strength ($10^{-8} - 0.5{\rm T}$), electron density ($10^6 - 10^{19}{\rm m}^{-3}$), wave frequency ($10^{-1} - 10^7{\rm Hz}$), as well as magnetic field configurations (dipole and tokamak geometry). As example, we examined fast compressional wave in Earth's magnetosphere and HHFW in the SOL of the tokamak. We also perform simulations using various boundary shapes for tokamak plasmas, which is beyond the previous full-wave AORSA code. Furthermore, the computational time of the FW2D code is short, for instance, it takes about 10 seconds for mesh number is 6000 and 15 minutes for mesh number 1e6 to get the results in Section III and Section IV, respectively, for a single processor.

We examined fast compressional wave propagation in the inner magnetosphere using the FW2D code is dramatically modified by a plasmaspheric plume. The results show that wave energy is trapped in the plume showing a leaky eigenmode-like structure with plume, which is consistent with to the detected magnetosonic waves from the satellites [36].

We also performed numerical simulations of HHFW in the SOL plasmas of NSTX/NSTX-U by adopting various boundaries. Comparison the results with previous full-wave simulations from AORSA code showed that although the FW2D code uses a cold plasma approximation, the electric field and the fraction of the power losses in the SOL plasmas show excellent consistency and agreement with each other. Similar to the AORSA simulations, the electric field amplitude and the fraction of the power losses in the SOL increase when the electron density in front of the antenna is large enough to open the FW cutoff. Therefore, the results in this paper confirm that the FW2D code produces the same power loss as AORSA.

We also adopted the vacuum vessel boundary into the FW2D. The initial results in this paper show the wave solution strongly depends on the boundary shape. For instance, when $N_{\rm ant}$ is slightly higher than $N_{\rm ec}$, HHFW cannot propagate to the SOL in the vacuum vessel as shown in Figure 6 while waves in the rectangular boundaries propagate to the SOL as shown in Figures 3 and 4. Therefore, these results suggest that realistic numerical domain should be considered in order to understand the wave propagation behavior as well as collisional power losses in the SOL. A more comprehensive work on this task will be published in a separate paper.

ACKNOWLEDGMENTS

The authors would like to thank Masayuki Ono and Stanley Kaye for their valuable comments. This material is based upon work supported by the U.S. Department of Energy, Office of Science, Office of Fusion Energy Sciences under contract number DE-AC02-09CH11466, SciDAC grant AT1030200, NASA grants 80HQTR18T0066, and also NSF grant AGS1602855.

[1] J. L. Rauch and A. Roux, J. Geophys. Res. **87**, 8191 (1982).
[2] K. Rönnmark and M. André, J. Geophys. Res. **96**, 17573 (1991).
[3] E.-H. Kim, J. R. Johnson, and D.-H. Lee, J. Geophys. Res. **113**, A11207. (2008).
[4] E.-H. Kim, I. H. Cairns, and P. A. Robinson, Phys. Rev. Lett. **99**, 15003 (2007).
[5] Y. Hu, R. E. Denton, and J. R. Johnson, J. Geophys. Res. **115**, 9218, doi:10.1029/2009JA015158 (2010).
[6] P. A. Damiano and J. R. Johnson, Geophys. Res. Lett. **39**, L02102 (2012).

[7] D.-H. Lee and R. L. Lysak, J. Geophys. Res. **94**, 17097 (1989).

[8] E.-H. Kim, J. R. Johnson, E. Valeo, and C. K. Phillips, Geophys. Res. Lett. **42**, 5147 (2015).

[9] E.-H. Kim and J. R. Johnson, Geophys. Res. Lett. p. doi:10.1002/2015GL066978 (2016).

[10] E.-H. Kim, N. Bertelli, E. Valeo, J. Hosea, R. Perkins, and J. R. Johnson, EPJ web of conference **157**, 02005 (2017).

[11] M. Ono, S. Kaye, Y.-K. Peng, G. Barnes, W. Blanchard, M. Cartera, J. Chrzanowski, L. Dudek, R. Ewigb, D. Gates, et al., Nucl. Fusion **40**, 557 (2000).

[12] S. Kaye, T. Abrams, J.-W. Ahn, J. Allain, R. Andre, D. Andruczyk, R. Barchfeld, D. Battaglia, A. Bhattacharjee, F. Bedoya, et al., Nucl. Fusion **55**, 104002 (2015).

[13] J. Hosea, R. E. Bell, B. P. LeBlanc, C. K. Phillips, G. Taylor, E. Valeo, J. R. Wilson, E. F. Jaeger, P. M. Ryan, J. Wilgen, et al., Phys. Plasmas **15**, 056104 (2008).

[14] C. Phillips, R. Bell, L. Berry, P. Bonoli, R. Harvey, J. Hosea, E. Jaeger, B. LeBlanc, P. Ryan, G. Taylor, et al., Nucl. Fusion **49**, 075015 (2009).

[15] G. Taylor, R. E. Bell, J. C. Hosea, B. P. LeBlanc, C. K. Phillips, M. Podesta, E. J. Valeo, J. R. Wilson, J.-W. Ahn, G. Chen, et al., Phys. Plasmas **17**, 056114 (2010).

[16] R. J. Perkins, J. C. Hosea, G. J. Kramer, J.-W. Ahn, R. E. Bell, A. Diallo, S. Gerhardt, T. K. Gray, D. L. Green, E. F. Jaeger, et al., Phys. Rev. Lett. **109**, 045001 (2012).

[17] R. Perkins, J.-W. Ahn, R. Bell, A. Diallo, S. Gerhardt, T. Gray, D. Green, E. Jaeger, J. Hosea, M. Jaworski, et al., Nucl. Fusion **53**, 083025 (2013).

[18] D. L. Green, L. A. Berry, G. Chen, P. M. Ryan, J. M. Canik, and E. F. Jaeger, Phys. Rev. Lett. **107**, 145001 (2011).

[19] N. Bertelli, E. Jaeger, J. Hosea1, C. Phillips, L. Berry, S. Gerhardt1, D. Green, B. LeBlanc, R. Perkins, P. Ryan, et al., Nucl. Fusion **54**, 083004 (2014).

[20] N. Bertelli, E. Jaeger, J. Hosea, C. Phillips, L. Berry, P. Bonoli, S. Gerhardt, D. Green, B. LeBlanc, R. Perkins, et al., Nuclear Fusion **56**, 016019 (2016).

[21] S. Shiraiwa, J. C. Wright, P. T. Bonoli, T. Kolev, and M. Stowell, EPJ Web of Conferences **157**, 03048, https://doi.org/10.1051/epjconf/201715703048 (2017).

[22] S. Shiraiwa, J. Wright, J. Lee, and P. Bonoli, Nucl. Fusion **57**, 086048, doi: 10.1088/1741 (2017).

[23] J. Wright and S. Shiraiwa, EPJ Web of Conferences **157**, 02011, https://doi.org/10.1051/epjconf/201715702011 (2017).

[24] E. F. Jaeger, L. A. Berry, E. DAzevedo, D. B. Batchelor, and M. D. Carter, Phys. Plasma **8**, 1573 (2001).

[25] J. Menard, J. Allain, D. Battaglia, F. Bedoya, R. Bell, E. Belova, J. Berkery, M. Boyer, N. Crocker, A. Diallo, et al., Nucl. Fusion **57**, 102006 (2017).

[26] M. Brambilla, Plasma Phys. Control. Fusion **41**, 1 (1999).

[27] N. E. Gibbs, W. G. J. Poole, and P. K. Stockmeyer, SIAM J. Numer. Anal. **13**, 236–250 (1976).

[28] P.-O. Persson and G. Strang, SIAM Review **46**, 329 (2004).

[29] J. R. Shewchuk, Computational Geometry **22**, 21 (2002).

[30] R. E. Denton, K. Takahashi, I. A. Galkin, P. A. Nsumei, X. Huang, B. W. Reinisch, R. R. Anderson, M. K. Sleeper, and W. J. Hughes, J. Geophys. Res. **111**, 04213 (2006).

[31] B. R. Sandel, J. Goldstein, D. L. Gallagher, and M. Spasojevic, Space Sci. Rev. **109**, 25 (2003).

[32] R. E. Denton, J. D. Menietti, J. Goldstein, S. L. Young, and R. R. Anderson, J. Geophys. Res. **109**, 09215 (2004).

[33] C. E. McIlwain, J. Geophys. Res. **66**, 3681 (1961).

[34] S. Gerhardt, R. Andre, and J. Menard, Nucl. Fusion **41**, 1 (2012).

[35] N. Bertelli, E. Jaeger, L. Berry, P. T. Bonoli, R. Budny, G.-Y. Fu, S. Gerhardt, D. L. Green, R. W. Harvey, J. C. Hosea, et al., AIP Conference Proceedings **1580**, 310, doi: 10.1063/1.4864550 (2014).

[36] Q. Ma, W. Li, L. Chen, R. M. Thorne, C. A.Kletzing, W. S. Kurth, G. B. Hospodarsky, G. D. Reeves, M. G. Henderson, and H. E.Spence, Geophys. Res. Lett **41**, 6307, doi:10.1002/2014GL061414 (2014).